remote sensing

MDPI

Article

A Hybrid Polarimetric Target Decomposition Algorithm with Adaptive Volume Scattering Model

Xiujuan Li [1], Yongxin Liu [2,*], Pingping Huang [3,4], Xiaolong Liu [3,4], Weixian Tan [3,4], Wenxue Fu [5] and Chunming Li [3,4]

[1] College of Computer Science, Inner Mongolia University, Hohhot 010021, China; lixiujuan@imut.edu.cn
[2] College of Electronic Information Engineering, Inner Mongolia University, Hohhot 010021, China
[3] College of Information Engineering, Inner Mongolia University of Technology, Hohhot 010051, China; hpp@imut.edu.cn (P.H.); liuxl@mail.bnu.edu.cn (X.L.); wxtan@imut.edu.cn (W.T.); lichunming@imut.edu.cn (C.L.)
[4] Inner Mongolia Key Laboratory of Radar Technology and Application, Hohhot 010051, China
[5] Aerospace Information Research Institute, Beijing 100094, China; fuwx@aircas.ac.cn
* Correspondence: yxliu@imu.edu.cn

Abstract: Previous studies have shown that scattering mechanism ambiguity and negative power issues still exist in model-based polarization target decomposition algorithms, even though deorientation processing is implemented. One possible reason for this is that the dynamic range of the model itself is limited and cannot fully satisfy the mixed scenario. To address these problems, we propose a hybrid polarimetric target decomposition algorithm (GRH) with a generalized volume scattering model (GVSM) and a random particle cloud volume scattering model (RPCM). The adaptive volume scattering model used in GRH incorporates GVSM and RPCM to model the volume scattering model of the regions dominated by double-bounce scattering and the surface scattering, respectively, to expand the dynamic range of the model. In addition, GRH selects the volume scattering component between GVSM and RPCM adaptively according to the target dominant scattering mechanism of fully polarimetric synthetic aperture radar (PolSAR) data. The effectiveness of the proposed method was demonstrated using AirSAR dataset over San Francisco. Comparison studies were carried out to test the performance of GRH over several target decomposition algorithms. Experimental results show that the GRH outperforms the algorithms we tested in this study in decomposition accuracy and reduces the number of pixels with negative powers, demonstrating that the GRH can significantly avoid mechanism ambiguity and negative power issues.

Keywords: hybrid polarimetric target decomposition; generalized volume scattering model (GVSM); random particle cloud model (RPCM); adaptive volume scattering model; polarimetric synthetic aperture radar (PolSAR)

Citation: Li, X.; Liu, Y.; Huang, P.; Liu, X.; Tan, W.; Fu, W.; Li, C. A Hybrid Polarimetric Target Decomposition Algorithm with Adaptive Volume Scattering Model. *Remote Sens.* **2022**, *14*, 2441. https://doi.org/10.3390/rs14102441

Academic Editors: Luis Gómez Déniz and Raydonal Ospina

Received: 5 April 2022
Accepted: 17 May 2022
Published: 19 May 2022

1. Introduction

Polarimetric target decomposition is a powerful technique used to interpret scattering mechanisms in polarimetric synthetic aperture radar (PolSAR) data and has been widely used in geological disaster monitoring [1,2], forest monitoring [3,4], soil moisture inversion [5,6], and land cover classification [7]. Many target decomposition techniques have been proposed over the past 20 years, and they can be mainly categorized into two groups. The first group is based on eigenvalues and eigenvectors of the coherency matrix [8]; although this kind of method provides mathematically unique results, some approximations have to be made to interpret the results in terms of known scattering mechanisms [9]. The second major group is based on the physical scattering model [10–13], which can obtain different decomposition solutions in terms of various scattering models. Meanwhile, conventional methods with models or assumptions that do not fit the observations may induce deficiencies [14], such as problems of volume scattering power overestimation or

generating pixels with negative powers. These deficiencies do not meet the minimum requirements that these model-based decomposition algorithms must satisfy [15,16]. Therefore, the development of effective model-based decompositions has received considerable attention, and many advances have been reported.

To improve the effectiveness of model-based methods, numerous studies have been carried out on scattering models. In early studies, volume scattering was modeled as randomly distributed needle-like particles, which hypothesizes that the parameters of one dimension of the particles approximate zero [17]. This assumption caused volume scattering power overestimation and some pixels with negative powers in the double-bounce scattering component or/and surface scattering component. Then, researchers improved the polarimetric target decomposition algorithms by optimizing the volume scattering models or adding extra scattering components. To optimize volume scattering models, researchers have proposed new volume scattering models by taking nonrandomly distributed particles into account [18] or proposed new volume scattering models to fit urban areas [19,20]. In terms of adding more scattering components, researchers developed the helix scattering model [21], wire scattering model [16], mixed dipole scattering model [22], $\pm 45^{\circ}$ oriented dipole scattering model, $\pm 45^{\circ}$ oriented quarter-wave reflectors [23], rotated dihedral scattering model [24], and disk-shaped random scatterers [25], et al. [26]. However, these scattering models are non-adaptive because they don't include any parameters that vary with the observed data, but the fact is that different targets perform different scattering mechanisms [27].

Therefore, scholars introduce an adaptive parameter to the scattering model [27,28]. One approach is to use machine learning methods to achieve optimal model selection. Chen et al. chose a model from four different volume scattering models with the minimum residual and then performed decomposition using the nonlinear least-squares algorithm [29]. Thomas et al. proposed a new approach to solve model-based decomposition by employing an L1-regularized optimization procedure, which automatically selected a set of optimal polarimetric scattering mechanisms and guaranteed nonnegative powers for the selected scattering mechanisms [30]. Another approach is to build physical models with adaptive properties. Van et al. used variable cylinders to model volume scattering in forest areas, which can distinguish forested and deforested land [31]; later, adaptive scattering models for forest areas and dihedral angle areas were proposed [32–35]. Xie et al. used a simplified Neumann volume scattering model to cover both random and nonrandom volume cases [36]. Wang et al. especially used the aggregation parameter to introduce the adaptive property into the division of needle-like particles to reduce the generation of negative power pixels [37]. Although the adaptive volume scattering model can adjust the coherency matrix or the covariance matrix automatically, all the above models, regardless of the effect of particle shape on scattering models, nor do they model the volume scattering for different scattering mechanisms dominant regions respectively [38], cause confusion in polarimetric target decomposition components or generate pixels with negative powers.

To address these issues, this paper proposes a novel hybrid polarimetric target decomposition algorithm named GRH based on an adaptive volume scattering model that is further composed of two models: the generalized volume scattering model (GVSM) and the random particle cloud model (RPCM). In contrast to previous models, the RPCM consists of particles with both shape and orientation rather than needle-like particles with a radius approximated to zero or distributed only in the radar plane of incidence. The adaptive volume scattering model in the GRH was determined during the procedure for polarimetric target decomposition calculation. Our tests on the L-band AirSAR dataset outperformed the existing popular/new polarimetric target decomposition algorithms. The GRH shows appreciable improvements in the decomposition component extraction accuracy compared with Freeman two-component decomposition (FRE2) [39], Yamaguchi four-component decomposition (YRO) [18], Yamaguchi four-component decomposition with rotation transformation (Y4R) [27], model-free four-component decomposition (MF4CF) [40] and hybrid

three-component decomposition (HTCD) [8]. The tests also shows that GRH yields a smaller percentage of pixels with negative powers than FRE2, YRO, Y4R, and HTCD.

2. Methodology

In this section, we calculated the coherency matrix in the radar line of sight direction using the polarimetric angle compensation method. Then, we used GVSM and RPCM to construct covariance matrices for the regions dominated by different scattering mechanisms, and eventually extracted decomposition components by solving the positive definite equations.

2.1. Orientation Angle Compensation

Orientation angle compensation (OAC) is a common polarimetric target decomposition data processing method used to minimize volume scattering components. The real unitary transformation (RUT) of a coherency matrix is introduced as the rotation of $\boldsymbol{T}$ about the line of sight by angle θ in [28]. The coherency matrix $\boldsymbol{T_0}$ of the line of sight radar can be defined as follows:

$$\boldsymbol{T_0} = \begin{bmatrix} T_{11}(\theta) & T_{12}(\theta) & T_{13}(\theta) \\ T_{21}(\theta) & T_{22}(\theta) & T_{23}(\theta) \\ T_{31}(\theta) & T_{32}(\theta) & T_{33}(\theta) \end{bmatrix} = \begin{bmatrix} 1 & 0 & 0 \\ 0 & cos2\theta & sin2\theta \\ 0 & -sin2\theta & cos2\theta \end{bmatrix} \boldsymbol{T} \begin{bmatrix} 1 & 0 & 0 \\ 0 & cos2\theta & -sin2\theta \\ 0 & sin2\theta & cos2\theta \end{bmatrix} \quad (1)$$

where $\boldsymbol{T}$ is the coherency matrix derived from measured fully PolSAR data.

$$\boldsymbol{T} = \begin{bmatrix} T_{11} & T_{12} & T_{13} \\ T_{21} & T_{22} & T_{23} \\ T_{31} & T_{32} & T_{33} \end{bmatrix} \quad (2)$$

To minimize the T_{33} term to constrain the problem of the volume scattering overestimation problem, it is necessary to rotate T_{33} to the position where its derivative is zero [27]

$$T_{33}(\theta) = T_{33}cos^2(2\theta) - Re(T_{23})sin(4\theta) + T_{22}sin^2(2\theta) \quad (3)$$

$$T'_{33}(\theta) = 2(T_{22} - T_{33})\ sin(4\theta) - 4\ Re(T_{23})cos(4\theta) \quad (4)$$

where $T'_{33}(\theta)$ is the derivative of $T_{33}(\theta)$, and the polarization angle θ was determined by $T'_{33}(\theta) = 0$, which corresponds to T_{33} with the minimum value when

$$tan(4\theta) = \frac{2Re(T_{23})}{T_{22} - T_{33}} \quad (5)$$

$$\theta = \frac{1}{4}tan^{-1}\left(\frac{2Re(T_{23})}{T_{22} - T_{33}}\right) \quad (6)$$

where $Re(T_{23})$ is the real part of T_{23}.

Then, the covariance matrix of the measured fully PolSAR data can be expressed as:

$$\boldsymbol{C} = \begin{bmatrix} C11 & C12 & C13 \\ C21 & C22 & C23 \\ C31 & C32 & C33 \end{bmatrix} = \boldsymbol{U_{L\_P}}\ \boldsymbol{T_0}\boldsymbol{U_{L\_P}^{-1}} \quad (7)$$

where

$$\boldsymbol{U_{L\_P}} = \frac{1}{\sqrt{2}}\begin{bmatrix} 1 & 0 & 1 \\ 1 & 0 & -1 \\ 0 & \sqrt{2} & 0 \end{bmatrix} \quad (8)$$

$$\boldsymbol{U_{L\_P}^{-1}} = \frac{1}{\sqrt{2}}\begin{bmatrix} 1 & 1 & 0 \\ 0 & 0 & \sqrt{2} \\ 1 & -1 & 0 \end{bmatrix} \quad (9)$$

The covariance matrix $\boldsymbol{C}$ we obtained in Equation (7) is to be further used in the following polarimetric target decomposition algorithms.

According to Maurya et al. [8], based on the sign of $(T_{11} - T_{22})$, either double-bounce or surface scattering was considered the dominant contribution in the measured fully PolSAR data. If $(T_{11} - T_{22}) \geq 0$, surface scattering is considered dominant; if $(T_{11} - T_{22}) < 0$, double-bounce scattering is considered dominant. In the following steps, we used the GVSM and the RPCM to model the volume scattering components of the regions dominated by the double-bounce scattering and the surface scattering, respectively.

2.2. Polarimetric Target Decomposition Algorithm for Regions Dominated by Double-Bounce Scattering

2.2.1. Volume Scattering Model for Regions Dominated by Double-Bounce Scattering

In a region where the double-bounce scattering mechanism is dominant, the volume scattering component is represented by the GVSM [38,41], and its covariance matrix can be expressed as:

$$\boldsymbol{C}_v = \frac{1}{1+e+r}\begin{bmatrix} r & 0 & p\sqrt{r} \\ 0 & e & 0 \\ p\sqrt{r} & 0 & 1 \end{bmatrix} \tag{10}$$

where

$$r = \frac{\sigma_{vvvv}}{\sigma_{hhhh}} \tag{11}$$

$$e = \frac{\sigma_{hvhv}}{\sigma_{vvvv}} \tag{12}$$

$$p = \frac{\sigma_{hhvv}}{\sqrt{\sigma_{hhhh}\sigma_{vvvv}}} \tag{13}$$

where σ_{vvvv} and σ_{hhhh} are the theoretical backscattering intensities of the co-polarized channel, σ_{hvhv} is the theoretical backscattering intensity of the cross-polarized channel of the scattering models, r and e are the intensity ratios, and p is the correlation coefficient of the horizontal polarization signal and vertical polarization signal. The parameters above are dependent on the physical parameters of the scattering model. Then, Ngiem et al. proposed [41]

$$e = \frac{1+r}{2} - p\sqrt{r} \tag{14}$$

Introducing (14) into (13) renders the following covariance matrix $\boldsymbol{C}_v$ for the volume scattering model:

$$\boldsymbol{C}_v = \frac{1}{\frac{3(1+r)}{2} - p\sqrt{r}}\begin{bmatrix} r & 0 & p\sqrt{r} \\ 0 & \frac{1+r}{2} - p\sqrt{r} & 0 \\ p^*\sqrt{r} & 0 & 1 \end{bmatrix} \tag{15}$$

In (15), the parameter p changes according to the scattering mechanism of the volume scattering model. To ensure that the GVSM represents the volume scattering caused by dipole and dihedral angle, p was selected according to the polarization characteristics of GVSM. The polarimetric scattering entropy (H) and polarimetric scattering $\overline{\alpha}$ parameter of GVSM are shown in Figure 1 for different p values.

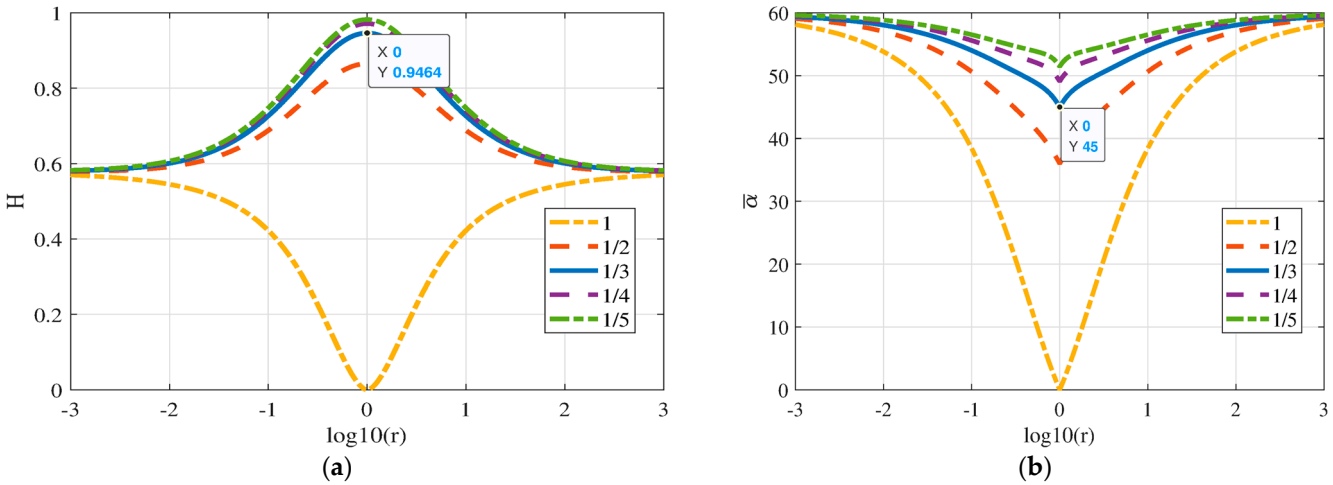

Figure 1. Polarization characteristics of GVSM. (**a**) H of GVSM with different p; (**b**) $\overline{\alpha}$ of GVSM with different p.

Without loss of generality, p was taken as 1, 1/2, 1/3, 1/4 and 1/5 to analyze the polarization characteristics of the GVSM, as shown in Figure 1. When $p > 1/3$, we set p to 1 and 1/2, and the corresponding $\overline{\alpha}$ ranged from 0° to 60° and from 36° to 60°, respectively. The scattering mechanism includes surface, dipole, and dihedral scattering. When $p < 1/3$, we set p to 1/4 and 1/5, and the corresponding $\overline{\alpha}$ ranged from 49.09° to 60° and 51.43° to 60°, and the scattering mechanism here does not include the dipole scattering mechanism. When $p = 1/3$, the range of $\overline{\alpha}$ was from 45° to 60°, which includes dipole and dihedral scattering. To model the volume scattering components of the regions dominated by double-bounce scattering, we chose the model with $p = 1/3$ (where $\overline{\alpha} \geq 45°$). For the model with $p = 1/3$, when $r = 1$, corresponding to $\overline{\alpha} = 45°$, the polarization entropy reaches its maximum value (0.9464); when r is far from 1, the value of $\overline{\alpha}$ will be greater than 45°, and the corresponding polarization entropy will decrease, as shown in Figure 1a,b. Therefore, the GVSM with $p = 1/3$ characterizes the polarization of the dihedral scattering mechanism and dipole scattering mechanism, and the covariance matrix $\boldsymbol{C_{3\_GVSM}}$ can be expressed as

$$\boldsymbol{C_{3\_GVSM}} = \frac{1}{\frac{3(1+r)}{2} - \frac{\sqrt{r}}{3}} \begin{bmatrix} r & 0 & \frac{\sqrt{r}}{3} \\ 0 & \frac{1+r}{2} - \frac{\sqrt{r}}{3} & 0 \\ \frac{\sqrt{r}}{3} & 0 & 1 \end{bmatrix} \tag{16}$$

2.2.2. Polarimetric Target Decomposition Algorithm with GVSM

For regions dominated by double-bounce scattering, the volume scattering was modeled using GVSM, and the second-order statistics covariance matrix $\boldsymbol{C_{3V\_GVSM}}$ is given by

$$\boldsymbol{C_{3V\_GVSM}} = f_V \boldsymbol{C_{3\_GVSM}} \tag{17}$$

where f_V corresponds to the volume scattering component contribution. According to FRE2, double-bounce scattering was modeled by the second-order statistics covariance matrix $\boldsymbol{C_{3G}}$ given by [39].

$$\boldsymbol{C_{3G}} = f_G \begin{bmatrix} 1 & 0 & \alpha \\ 0 & 0 & 0 \\ \alpha^* & 0 & |\alpha|^2 \end{bmatrix} \tag{18}$$

where f_G corresponds to the double-bounce scattering component contribution in this case. Then, the covariance matrix $\boldsymbol{C}$ of the measured fully PolSAR data can be expressed as:

$$\boldsymbol{C} = \boldsymbol{C_{3G}} + \boldsymbol{C_{3V\_GVSM}} = \begin{bmatrix} \frac{f_V}{k}.r + f_G & 0 & \frac{f_V}{k}.\frac{\sqrt{r}}{3} + \alpha f_G \\ 0 & \frac{f_V}{k}\left(\frac{(1+r)}{2} - \frac{\sqrt{r}}{3}\right) & 0 \\ \frac{f_G}{k}.\frac{\sqrt{r}}{3} + \alpha^* f_G & 0 & \frac{f_V}{k} + |\alpha|^2 f_G \end{bmatrix} \tag{19}$$

There are four unknowns, namely f_V, f_G, α, and r, where α is a complex number and the other unknowns are real numbers, with

$$k = \frac{3(1+r)}{2} - \frac{\sqrt{r}}{3} \tag{20}$$

Then, we obtained four equations according to Equations (7) and (19):

$$\begin{cases} \frac{f_V}{k}(\frac{(1+r)}{2}) - \frac{\sqrt{r}}{3})^2 = C22 & (a) \\ \frac{f_V}{k} \cdot r + f_G = C11 & (b) \\ \frac{f_V}{k} \cdot \frac{\sqrt{r}}{3} + \alpha f_G = C13 & (c) \\ \frac{f_V}{k} + |\alpha|^2 f_G = C33 & (d) \end{cases} \tag{21}$$

We set

$$m_0 = \frac{(1+r)}{2} - \frac{\sqrt{r}}{3} \tag{22}$$

then

$$f_V = \frac{kC22}{m_0} \tag{23}$$

$$f_G = C11 - \frac{C22}{m_0} r \tag{24}$$

We name

$$\alpha = y + zj \tag{25}$$

Then, from Equation (21) (c), we have

$$y = \frac{Re(C13)m_0 - C22\frac{\sqrt{r}}{3}}{C11m_0 - C22r} \tag{26}$$

$$z = \frac{Im(C13)}{C11m_0 - C22r} \tag{27}$$

After polynomial elimination calculations, we obtained a unary quartic equation of $\sqrt{r}$ as

$$a\left(\sqrt{r}\right)^4 + b\left(\sqrt{r}\right)^3 + c\left(\sqrt{r}\right)^2 + d\sqrt{r} + e = 0 \tag{28}$$

where

$$a = \frac{1}{4}\left(|C13|^2 - C11C33 + 2C22C33\right) \tag{29}$$

$$b = -\frac{1}{3}(|C13|^2 + Re(C13)C22 - C11C33 + C22C33) \tag{30}$$

$$c = \frac{1}{2}(C11C22 + C22C33) + \frac{11}{18}\left(|C13|^2 - C11C33\right) + \frac{1}{9}\left(C_{22}^2 + 2Re(C13)C22\right) \tag{31}$$

$$d = -\frac{1}{3}(C11C22 + |C13|^2 + Re(C13)C22 - C11C33) \tag{32}$$

$$e = \frac{1}{2}C11C22 + \frac{1}{4}|C13|^2 - C11C33 \tag{33}$$

By solving Equation (28) using the Ferrari formulas, we obtained four roots. Among the four roots, we needed to choose one root to determine the volume scattering model to calculate the volume scattering component of the measured fully PolSAR data. The root was selected based on the characteristics of the volume scattering model, as shown in Figure 1b, and the value of r with the closest $\overline{\alpha}$ to 45° was selected as the final root. If the obtained $\sqrt{r}$ had multiple valid roots ($\sqrt{r} > 0$), the minimum of $abs(\log_{10} r)$ was selected as the final resultant value. Subsequently, the volume scattering power and double-bounce scattering power can be calculated as follows:

$$P_V = \frac{f_V}{k}(r + m_0 + 1) \tag{34}$$

$$P_d = f_G\left(1 + |\alpha|^2\right) \tag{35}$$

2.3. Polarimetric Target Decomposition Algorithm for Regions Dominated by Surface Scattering

2.3.1. Volume Scattering Model for Regions Dominated by Surface Scattering

For regions dominated by surface scattering, volume scattering component was characterized by RPCM [9,42]; in contrast to the Freeman–Durden and Yamaguchi volume scattering model, we no longer assumed one dimension of the particles approximated to zero, and we took the shape of the particles into account instead. The particle-specific parameters were determined based on the measured fully PolSAR data. The geometric model of a single ellipsoidal particle in the Cartesian coordinate system is shown in Figure 2.

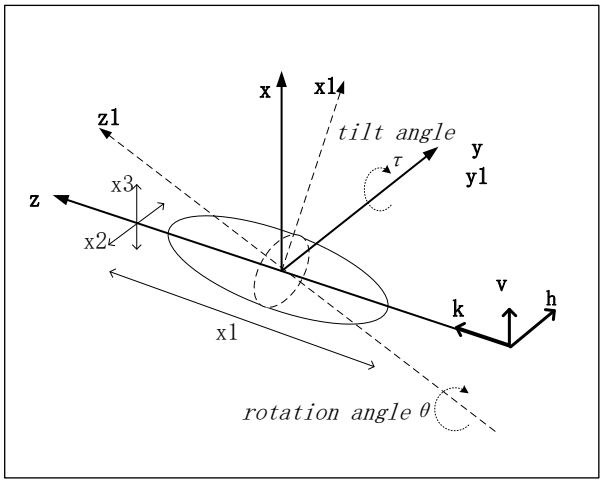

Figure 2. Ellipsoidal particle model in the Cartesian coordinate system.

Given an ellipsoidal scatterer with axes x1, x2, x3 (x1 > x2 = x3); and Eulerian tilt and rotation angles of τ and θ, respectively, relative to the radar line of sight 'k', both τ and θ are within the range of [0, 180]. The initial position of the ellipsoid was located at the position where both τ and θ are zero. To obtain the ellipsoidal particle with arbitrary orientation distribution in space, the ellipsoidal particle was rotated as follows: first, the ellipsoidal particle was rotated by an inclination angle τ on the x coordinate direction of the Cartesian coordinate system to obtain the position in the new coordinate system (x1, y1, z1), and then the ellipsoidal particle was rotated by an angle of θ on the y1 coordinate axis direction on the x1 axis around the z1 axis. After the two rotations above, we obtained an ellipsoidal particle with an arbitrary angle. Under the assumption that each particle is independent, we considered only single scattering, and the backscattering coefficient matrix can be expressed in terms of the physical particle characteristics as

$$S = \begin{bmatrix} s_{11} & s_{12} \\ s_{21} & s_{22} \end{bmatrix} \tag{36}$$

According to the reciprocity principle, the two cross-polarizations were considered equal; that is, $s_{12} = s_{21}$, where

$$s_{11} = cos^2\theta sin^2\tau + Asin^2\theta + Acos^2\theta cos^2\tau \tag{37}$$

$$s_{22} = sin^2\theta sin^2\tau + Acos^2\theta + Asin^2\theta cos^2\tau \tag{38}$$

$$s_{12} = \left(sin^2\tau - A + Acos^2\tau\right)cos\theta sin\theta \tag{39}$$

As shown above, the scattering coefficient matrix of the random ellipsoidal particle can be expressed in terms of the particle anisotropy degree A for its shape, and the Euler angles τ and θ to represent the orientation of the particle. In the single-station backward scattering regime, the polarization scattering matrix satisfied reciprocity, and the Pauli basis vector for the scattering target obtained from the matrix $\boldsymbol{S}$ can be expressed as:

$$K = \frac{1}{\sqrt{2}}\begin{bmatrix} s_{11} + s_{22} & s_{11} - s_{22} & 2s_{12} \end{bmatrix}^T \tag{40}$$

The coherency matrix can be calculated as:

$$\boldsymbol{T} = \langle K * K^{*T} \rangle = \frac{1}{2}\langle \begin{bmatrix} (s_{11} + s_{22})^2 & {s_{11}}^2 - {s_{22}}^2 & 2(s_{11} + s_{22})s_{12} \\ {s_{11}}^2 - {s_{22}}^2 & (s_{11} - s_{22})^2 & 2(s_{11} - s_{22})s_{12} \\ 2(s_{11} + s_{22})s_{12} & 2(s_{11} - s_{22})s_{12} & 4{s_{12}}^2 \end{bmatrix} \rangle \tag{41}$$

The coherency matrix elements in Equation (41) are all functions of θ and τ, which are denoted as $t_{ij}(\theta, \tau)$. Then, the overall average coherency matrix elements $\langle t_{ij} \rangle$ of the randomly distributed ellipsoidal particles in the direction perpendicular to the radar line of sight can be obtained by integrating $t_{ij}(\theta, \tau)\sin\tau$ over all angles, as follows:

$$T_{ij\_RPCM} = \langle t_{ij} \rangle = \frac{1}{4\pi}\int_{-\Theta}^{\Theta}\int_{0}^{\pi} t_{ij}(\theta, \tau)\, \sin\tau d\tau d\theta \tag{42}$$

where $1/4\pi$ is the normalization factor, the range of τ is [0, 180°] and the range of θ is limited to $[-\Theta,\Theta]$. First, we considered only the case of the random ellipsoidal particle cloud at τ = 90°, and the ellipsoidal particle orientation can be in any direction in the radar sight plane. The range of θ was limited to $-90° < \theta < 90°$ via ellipsoidal particle symmetry, so Equation (42) yielded the coherency matrix elements as:

$$T_{11\_RPCM} = (A + 1)^2 \tag{43}$$

$$T_{22\_RPCM} = \frac{1}{2}(A - 1)^2 \tag{44}$$

$$T_{33\_RPCM} = \frac{1}{2}(A - 1)^2 \tag{45}$$

Then, the coherency matrix of the new volume scattering model can be obtained as:

$$\boldsymbol{T_{3\_RPCM}} = \begin{bmatrix} (A + 1)^2 & 0 & 0 \\ 0 & \frac{1}{2}(A - 1)^2 & 0 \\ 0 & 0 & \frac{1}{2}(A - 1)^2 \end{bmatrix} \tag{46}$$

The corresponding covariance matrix $\boldsymbol{C_{3\_RPCM}}$ is

$$\boldsymbol{C_{3\_RPCM}} = \boldsymbol{U_{L\_P}^{-1}}\boldsymbol{T_{3V\_RPCM}}\boldsymbol{U_{L\_P}} = \frac{1}{2}\begin{bmatrix} (A + 1)^2 + \frac{1}{2}(A - 1)^2 & 0 & (A + 1)^2 - \frac{1}{2}(A - 1)^2 \\ 0 & (A - 1)^2 & 0 \\ (A + 1)^2 - \frac{1}{2}(A - 1)^2 & 0 & (A + 1)^2 + \frac{1}{2}(A - 1)^2 \end{bmatrix} \tag{47}$$

2.3.2. Polarization Decomposition Algorithm with RPCM

For surface scattering dominant regions, the volume scattering was modeled using the above RPCM, and the second-order statistics covariance matrix $\boldsymbol{C_{3V\_RPCM}}$ is given by

$$\boldsymbol{C_{3V\_RPCM}} = f_V \boldsymbol{C_{3\_RPCM}} \tag{48}$$

The surface scattering was also modeled using FRE2, as shown in Equation (18), where f_G corresponds to the surface scattering component contribution in this case. The covariance matrix $\boldsymbol{C}$ of the measured fully PolSAR data can be expressed as:

$$\boldsymbol{C} = \boldsymbol{C_{3G}} + \boldsymbol{C_{3V\_RPCM}} = \begin{bmatrix} \frac{1}{4}\left(2(A+1)^2 + (A-1)^2\right)f_V + f_G & 0 & \frac{1}{4}\left(2(A+1)^2 - (A-1)^2\right)f_V + \alpha f_G \\ 0 & \frac{1}{2}(A-1)^2 f_V & 0 \\ \frac{1}{4}\left(2(A+1)^2 - (A-1)^2\right)f_V + \alpha^* f_G & 0 & \frac{1}{4}\left(2(A+1)^2 + (A-1)^2\right)f_V + |\alpha|^2 f_G \end{bmatrix} \tag{49}$$

Then, the four equations can be formulated according to Equations (7) and (49):

$$\begin{cases} \frac{1}{2}(A-1)^2 f_V = C22 & (a) \\ \frac{1}{2}(A+1)^2 f_V + \frac{1}{4}(A-1)^2 f_V + f_G = C11 & (b) \\ \frac{1}{2}(A+1)^2 f_V - \frac{1}{4}(A-1)^2 f_V + \alpha f_G = C13 & (c) \\ \frac{1}{2}(A+1)^2 f_V + \frac{1}{4}(A-1)^2 f_V + \left|\alpha\right|_2 f_G = C33 & (d) \end{cases} \tag{50}$$

By solving the above equations, we obtained

$$f_G = \frac{Im^2(C13) + (Re(C13) - C11 - C22)^2}{C33 - 2Re(C13) - C22 + C11} \tag{51}$$

from Equation (50) (c)

$$Im(\alpha) = Im(C13)/f_G \tag{52}$$

$$Re(\alpha) = (Re(C13) + C22 - C11)\frac{1}{f_G} + 1 \tag{53}$$

We set

$$K = \frac{1}{2}(A+1)^2 f_V = C11 - \frac{1}{2}C22 - f_G \tag{54}$$

then

$$A = \frac{(2K + 2C22) \pm \sqrt{4(K + C22)^2 - 4(K - C22)^2}}{2(K - C22)} \tag{55}$$

There are two roots for Equation (55), which are denoted as $A1$ and $A2$. According to the physical characteristics of the RPCM, the shape approached the dipole, while A was farther from 1. Therefore, the value of A was taken as shown in Table 1.

Table 1. A-value selection strategy.

	$A2 > 0$	$A2 < 0$
$A1 > 0$	$max(\lvert\log_{10} A1\rvert, \lvert\log_{10} A2\rvert)$	$A1$
$A2 < 0$	$A2$	Nan

In addition, where f_V is positive, $K > 0$.

Subsequently, the volume scattering power and the surface scattering power can be calculated as follows:

$$P_V = 2(C22 + K) \tag{56}$$

$$P_S = f_G\left(1 + |\alpha|^2\right) \tag{57}$$

2.4. Hybrid Polarimetric Target Decomposition Algorithm with Adaptive Volume Scattering Model

According to the dominant scattering mechanisms of different regions, the corresponding volume scattering model was selected to build the hybrid polarization decomposition algorithm with the following steps:

1. Extract coherency matrix $\boldsymbol{T}$ from the measured fully PolSAR data using PolSARpro software;
2. Boxcar filtering with an 3×3 window for the elements of the coherency matrix to reduce speckle noise;
3. Calculate the polarization angle using T_{22}, the real part of T_{23}, and T_{33} according to Equation (6), and obtain the scattering matrix $\boldsymbol{T_0}$ in the radar line of sight direction following Equation (1);
4. Calculate the covariance matrix $\boldsymbol{C}$ by converting the coherency matrix $\boldsymbol{T_0}$ following Equation (7);
5. Determine the dominant scattering mechanism for each pixel using the relationship between T_{11} and T_{22}. The pixel will be surface scattering dominant when $(T_{11} - T_{22}) \geq 0$; otherwise, double-bounce scattering will be dominant;
6. Calculate the polarimetric target decomposition components using the corresponding polarimetric target decomposition algorithms according to the different scattering mechanisms to obtain the value of each scattering component of each pixel.

3. Experimental Results and Discussion

Our intention in this study was to improve the decomposition algorithm by developing an adaptive volume scattering model. We first compared the scattering characteristics of the GVSM, RPCM and other commonly used volume scattering models to illustrate the theoretical feasibility of our proposed algorithm, GRH. To verify the effectiveness of the GRH, experiments were conducted on the L-band AirSAR dataset near the Golden Gate Bridge in San Francisco. The effectiveness of the GRH was evaluated based on two factors [8,10].

1. Accuracy in the decomposition component;
2. Percentage of negative power pixels.

3.1. Theoretical Feasibility of the Adaptive Volume Scattering Model

The polarimetric scattering entropy (H) and polarimetric scattering $\overline{\alpha}$ parameter are important parameters used to study the scattering properties of observation targets. The entropy H is a measure of the randomness of scattering mechanisms, and the parameter $\overline{\alpha}$ identifies the dominant scattering mechanism [43]. The reasonable ranges for H and $\overline{\alpha}$ are [0, 1] and [0°, 90°], respectively. The two-dimensional $H/\overline{\alpha}$ plane contains nine sections, each related to specific scattering characteristics that can be measured by the coherency, the position of the values of H and $\overline{\alpha}$, indicating different types of targets. On the $H/\overline{\alpha}$ plane, $H = 0$ and $\overline{\alpha} = 0°$ correspond to surface scattering, while $H = 0$ and $\overline{\alpha} = 45°$ indicate dipole scattering with a cloud of anisotropic particles, which has the maximum entropy when following the random distribution, where $H = 0$ and $\overline{\alpha} = 90°$ correspond to dihedral scattering from metallic surfaces [44].

The H and $\overline{\alpha}$ variation curves of the GVSM, RPCM and FRE2 volume scattering model are shown in Figure 3. The horizontal axes of the plots reflect the parameters representing the scattering particle aspect ratio: r for GVSM, A for RPCM, and η for FRE2 volume scattering model. The vertical axes are the polarimetric scattering entropy (H) and polarimetric scattering $\overline{\alpha}$ parameter.

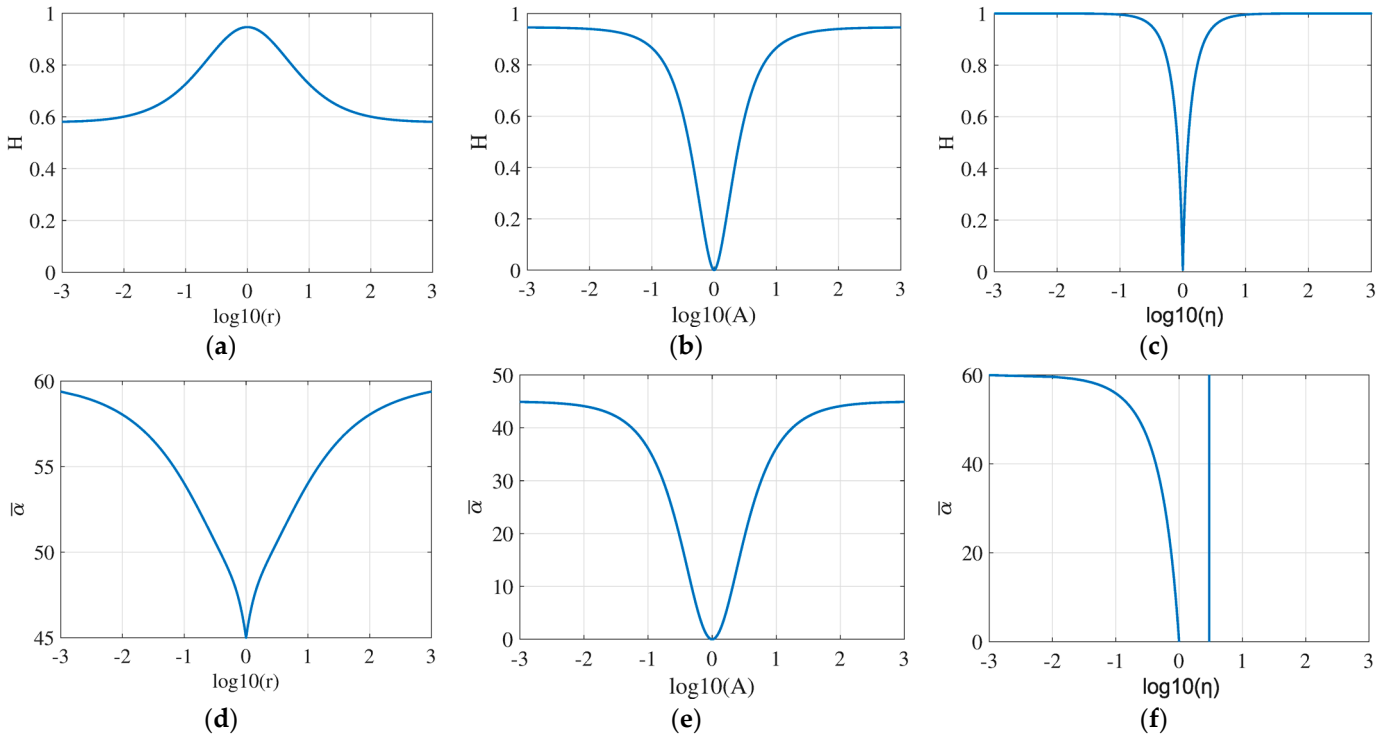

Figure 3. H and $\overline{\alpha}$ of the volume scattering model. (**a**) H of GVSM; (**b**) H of RPCM; (**c**) H of FRE2 volume model; (**d**) $\overline{\alpha}$ of GVSM; (**e**) $\overline{\alpha}$ of RPCM; (**f**) $\overline{\alpha}$ of FRE2 volume model.

For the GVSM in Figure 3a,d, $\overline{\alpha}$ changes from 60° to 45°, which contains the scattering mechanisms of dihedral scattering and dipole scattering; when $r = 1$, $\overline{\alpha}$ and H will be 45° and 0.9464, respectively, indicating dipole scattering; when r is far from 1, the scattering characteristics will be close to dihedral scattering, and the value of H decreases correspondingly.

For the RPCM in Figure 3b,e, $\overline{\alpha}$ changes from 45° to 0°, which contains both scattering mechanisms of dipole and surface scattering. When $A = 1$, the shape of the particles is close to a sphere; as is well known, the scattering mechanism of a sphere is surface scattering, where $H = 0$ and $\overline{\alpha} = 0$. When A is far from 1, the shape of the particles becomes thinner, and $\overline{\alpha}$ and H will be 45° and 0.9464, respectively, which is equal to the maximum value of the GVSM, with $p = 1/3$. Thus, RPCM can now be considered random dipole scattering, such as the volume scattering model of Freeman–Durden three-component decomposition (FDD) [17].

For the FRE2 volume scattering model shown in Figure 3c,f, when $\eta < 1$, $\overline{\alpha}$ changes from 60° to 0°, which contains all scattering mechanisms of dihedral angle, dipole, and surface scattering, while when $\eta \geq 1$, $\overline{\alpha}$ no longer varies with the parameter η, and parameter $\overline{\alpha}$ will be out of the valid value range. When $\overline{\alpha} \geq 60°$, the entropy H corresponds to the maximum value of 1.

The above volume scattering models are all adaptive volume scattering models, and their scatterplot on the two-dimensional $H/\overline{\alpha}$ plane can be obtained from the above H, $\overline{\alpha}$, as shown in Figure 4. There are also some commonly used volume scattering models that are nonadaptive scattering models, such as the YRO volume scattering model [18], An's volume scattering model [45], and FDD volume scattering model [17], for which H and $\overline{\alpha}$ are all fixed values. The polarimetric scattering characteristics of those volume scattering models are also shown in Figure 4. The relationship between these volume scatting models can be found as follows:

- The polarimetric scattering characteristic line of GVSM (in red line) is in Zones 5, 4 and 2 of the $H/\overline{\alpha}$ plane. Among them, Zone 5 is medium entropy vegetation scattering, Zone 4 is medium entropy multiple scattering, and Zone 2 is high entropy vegeta-

tion scattering. This means that the GVSM can represent double-bounce scattering mechanisms and volume scattering mechanisms;

- The polarimetric scattering characteristic line of RPCM (in blue line) overlaps with the boundary line of the two-dimensional $H/\overline{\alpha}$ plane (in black line); they are in Zones 9, 6, and 2 of the $H/\overline{\alpha}$ plane. Among these zones, Zone 9 has a low entropy surface scatter, and Zone 6 has a medium entropy surface scatter, which means that the RPCM scan represents both surface scattering and volume scattering;
- The lower left part of the FRE2 volume scattering model polarimetric scattering characteristic line (in gray) overlaps with the RPCM polarimetric scattering characteristic line (in blue) and the boundary line of the two-dimensional $H/\overline{\alpha}$ plane (in black line). The upper part of the FRE2 volume scattering model polarimetric scattering characteristic line (in gray) drops out of the two-dimensional $H/\overline{\alpha}$ plane, and the right part of the characteristic line is irregular;
- The FDD volume scattering model (the red pentagram in Zone 2) is at the intersection point of the GVSM line and RPCM line, indicating that the FDD volume scattering model is a special case of these two models;
- The YRO volume scattering model (the blue diamond in Zone 4) is at the edge of the polarimetric scattering characteristic line of GVSM (in red), showing that the YRO volume scattering model is a special case of GVSM;
- An's volume scattering model (black star in Zone 1) is a completely random model located on the right tip point of the $H/\overline{\alpha}$ plane, which belongs to high entropy multiple scattering and overlaps with points of the FRE2 volume scattering model.

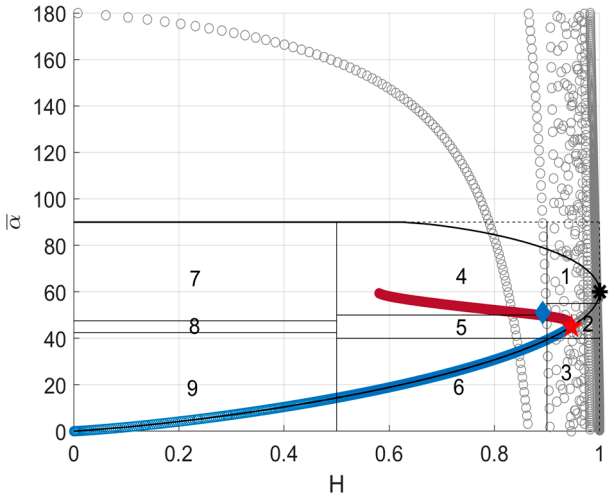

Figure 4. Two-dimensional $H/\overline{\alpha}$ plane of volume scattering models: FRE2 volume scattering model: gray line; GVSM: red line; RPCM: blue line; FDD volume scattering model: red pentagram; YRO volume scattering model: blue diamond; An's volume scattering model: black star.

In summary, the YRO, FDD and An's volume scattering models cannot adjust to the measured fully PolSAR data and are unable to accurately characterize the volume scattering of the observed targets. The FRE2 volume scattering model considers all scattering mechanisms, but there are irrational situations, such as the right part of the characteristic line in Figure 4. Although GVSM can characterize double-bounce and volume scattering, it fails to characterize surface scattering, while RPCM can characterize surface scattering and volume scattering but fails to characterize double-bounce scattering. Therefore, we combined GVSM and RPCM to build an adaptive volume scattering model that has a larger adaptive dynamic range. Its useful range covers the surface, encompassing dipole and double-bounce scattering. Meanwhile, the model can be selected appropriately according to the dominant scattering mechanism of the data.

The above analysis shows that the adaptive volume scattering model based on the GVSM and RPCM proposed in this paper has more reasonable polarization scattering characteristics than other commonly used volume scattering models, illustrating its theoretical feasibility. In the following section, we analyze the effectiveness of GRH using the measured fully PolSAR dataset.

3.2. Experiments on the AirSAR Dataset

The L-band AirSAR dataset used in this paper was a 4-look measured fully PolSAR dataset with a spatial resolution of 10 m and an incidence angle of 5°–60° [11]. The data were downloaded from the Institute of Electronics and Telecommunications of Rennes (IETR) (URL: https://ietr-lab.univ-rennes1.fr/polsarpro-bio/san-francisco/, accessed on 2 December 2021). The original image was 900 × 1024 pixels, and the Pauli pseudo-color image is shown in Figure 5.

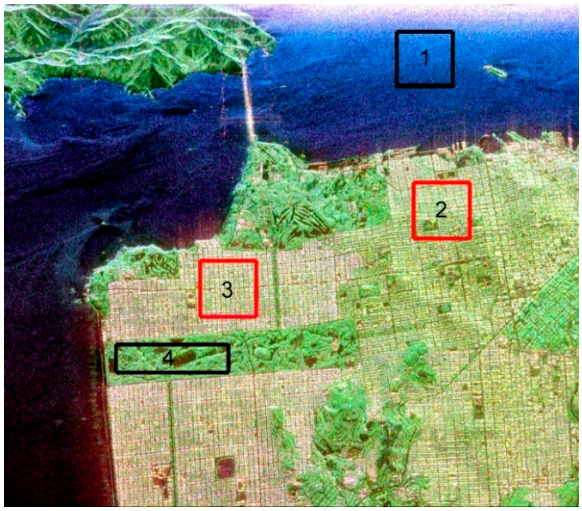

Figure 5. Pauli pseudo-color image of the AirSAR data.

The regions in Figure 5 labeled with rectangles were used to demonstrate the effectiveness of the proposed method. For convenience, hereinafter, we named the four selected regions as Zone 1, Zone 2, Zone 3, and Zone 4. These regions were chosen to cover different land covers featuring different but representative scattering characteristics. Zone 1 was the ocean area that is considered strong surface scattering targets, Zone 2 and Zone 3 were the city blocks that have strong double-bounce scattering characteristics, and Zone 4 was the vegetation area where mainly volume scattering occurs. The sizes of Zones 1, 2, 3, and 4 were 100 × 100 pixels, 100 × 100 pixels, 100 × 100 pixels, and 50 × 200 pixels, respectively.

We used AirSAR data to compare the performance of GRH with that of FRE2, YRO, Y4R, MF4CF and HTCD, among which FRE2, YRO and Y4R are classic algorithms, while MF4CF and HTCD are relatively new. The pseudo-color images generated from these six algorithms are shown in Figure 6. The color of each pixel is determined by double-bounce scattering power (Pd), volume scattering power (Pv) and surface scattering power (Ps) together, where Pd, Pv and Ps correspond to red, green and blue, so the color presented by each pixel represents the intensity of the three scattering components corresponding to that element. The color of the figure can be used for visual interpretation.

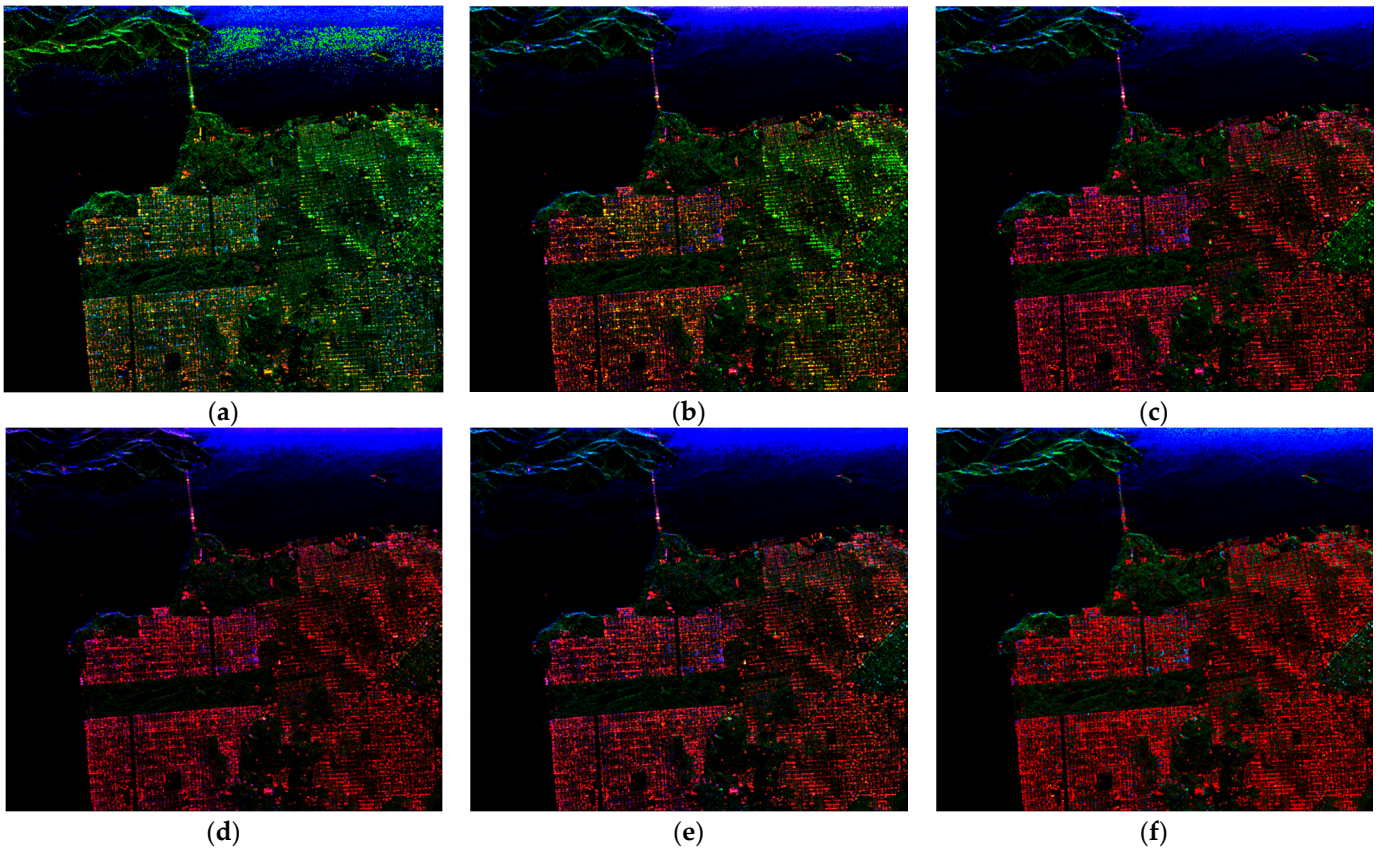

Figure 6. Pseudo-color images of the polarimetric target decomposition results. Red: double-bounce scattering (*Pd*); Green: volume scattering (*Pv*); Blue: surface scattering (*Ps*). (**a**) FRE2; (**b**) YRO; (**c**) Y4R; (**d**) MF4CF; (**e**) HTCD; (**f**) GRH.

The decomposition result of GRH is shown in Figure 6f. Compared with the five existing methods, it seems more red in urban areas and bridge areas, more green in vegetation areas than most other algorithms and more blue in ocean areas than FRE2. Specifically, as shown in Figure 6a, FRE2 decomposition had a serious problem of volume scattering overestimation in both urban and ocean areas; YRO also had a problem with volume scattering overestimation in urban areas, as shown in Figure 6b. For Figure 6c, Y4R had a more reasonable performance in all three scattering regions and could distinguish the three different scattering mechanisms on the image; however, the urban area was less red than the GRH, especially in the upper left part of the urban area. MF4CF decomposition in Figure 6d appears red in the urban area but darker in the vegetation area. For the HTCD decomposition shown in Figure 6e, there were many volume scattering components in the upper left part of the urban area. The GRH in Figure 6f had good performance in all three scattering regions and the best performance in detailed feature extraction, such as the bridge and the ship. The visual assessment showed that the GRH outperformed the other methods in our tests.

To quantitatively evaluate the performance of the scattering component extraction accuracy, we calculated the scattering power of the AirSAR data as shown in Table 2. The GRH had a preferable result over the other five algorithms. The double-bounce scattering component of GRH increased by 27.35%, 17.19%, 5.95%, and 6.90% over FRE2, YRO, Y4R, and HTCD, respectively, and decreased by 1.05% over MF4CF. Although MF4CF's double-bounce scattering was higher than that of the GRH, it can be seen in Figure 6d that it had the problem of the underestimation of volume scattering because the boat demonstrated typical dipole scattering, which belongs to the volume scattering mechanism, but as shown in Figure 6d, it was characterized by surface scattering, so that we could hardly see it in the

image. The volume scattering component contribution obtained via the GRH decreased over FRE2, YRO, and Y4R and increased in the double-bounce scattering component over the whole image. The volume scattering component decreased by 29.98%, 13.15%, and 0.37% over FRE2, YRO, and Y4R, and increased by 7.69% and 3.91% over MF4CF and HTCD, respectively. The surface scattering decreased by 4.04%, 5.58%, 6.64%, and 10.81% over YRO, Y4R, MF4CF, and HTCD, respectively, and increased by 2.63% over FRE2.

Table 2. The percentage of every polarization decomposition component for each algorithm (%).

Component	FRE2	YRO	Y4R	MF4CF	HTCD	GRH
Pd	8.47	18.63	29.87	36.87	28.92	35.82
Pv	52.25	35.42	22.64	14.58	18.36	22.27
Ps	39.28	45.95	47.49	48.55	52.72	41.91

Therefore, the results of the quantitative analysis are consistent with the visual assessment described above.

To further evaluate the performance of the proposed method in regions dominated by different scattering, we selected the four regions delineated in Figure 5 to analyze the decomposition component extraction accuracy. We marked urban areas dominated by double-bounce scattering as Mask_1 (Zones 2 and 3), vegetated areas dominated by volume scattering as Mask_2 (Zone 4), and ocean areas dominated by surface scattering as Mask_3 (Zone 1). The percentage of each decomposition component of all methods in the three masks is listed in Table 3.

Table 3. The percentage of each polarization component of all methods in the three masks (%).

Region	Component	FRE2	YRO	Y4R	MF4CF	HTCD	GRH
Mask_1	*Pd*	12.48	34.19	69.52	83.05	64.93	72.78
	Pv	78.72	58.13	19.19	9.23	16.89	23.74
	Ps	8.79	7.68	11.29	7.72	18.18	3.48
Mask_2	*Pd*	2.25	6.07	7.77	19.75	8.36	16.11
	Pv	87.85	86.93	82.80	66.30	71.12	78.03
	Ps	9.89	7.00	9.43	13.95	20.52	5.86
Mask_3	*Pd*	0.00	0.00	0.00	0.00	0.00	0.00
	Pv	26.03	0.00	0.00	0.00	0.00	0.00
	Ps	73.97	1.00	1.00	1.00	1.00	1.00

According to Table 3, the percentage of each polarization component in the regions dominated by different scattering mechanisms is shown in Figure 7. Figure 7a shows that the double-bounce scattering of the GRH was higher than that of the other methods in urban areas (Mask_1), except MF4CF, and most of the pixels in this area showed double-bounce scattering. Figure 7b shows that the volume scattering of the GRH was lower than that of FRE2, YRO, and Y4R, but higher than that of HTCD and MF4CF in the vegetation area (Mask_2). Electromagnetic waves in the L-band could penetrate the vegetation canopy and reach the ground, resulting in double-bounce scattering between the ground surface and the tree trunk, so there were double-bounce scattering-dominated pixels in this area, but the dominant scattering mechanism in this region was still volume scattering. Mask_3 is an ocean area with pure surface scattering, and pixels of this area were occupied by surface scattering for YRO, Y4R, MF4CF, HTCD and GRH decomposition results; however, FRE2 had a volume scattering overestimation problem for this area.

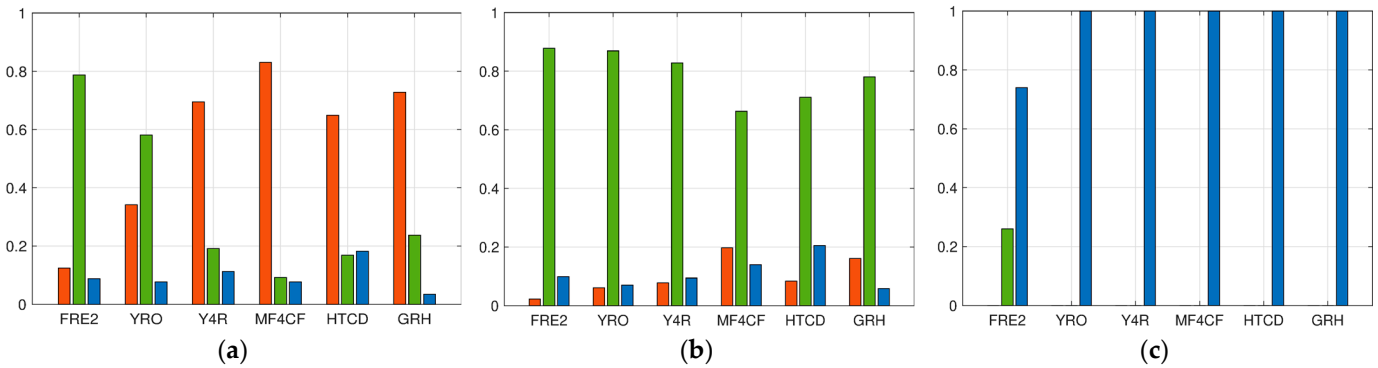

Figure 7. Bar charts of polarimetric target decomposition results. Red: double-bounce scattering (*Pd*). Green: volume scattering (*Pv*). Blue: surface scattering (*Ps*). (**a**) Results of decomposition of urban area; (**b**) Results of decomposition of vegetation area; (**c**) Results of decomposition of ocean area.

In summary, GRH was more consistent with the actual scattering mechanism of the scattering targets than the other algorithms and had a more accurate scattering component extraction capability. Combined with Figure 6, the algorithm proposed in this paper had the best scattering feature extraction accuracy compared with the other algorithms in the overall view.

In addition, the occurrence of negative scattering powers is an important indicator to evaluate the performance of polarimetric target decomposition algorithms [10]. The percentages of the negative power pixels obtained via the aforementioned six decomposition methods for the AirSAR data we used are listed in Table 4.

Table 4. The percentage of negative power pixels for each algorithm (%).

Component	FRE2	YRO	Y4R	MF4CF	HTCD	GRH
Pd	5.78	18.09	17.75	0.00	15.64	0.00
Pv	15.59	0.00	0.00	0.00	0.00	0.00
Ps	2.09	15.96	5.42	0.00	0.95	0.00
Total	23.46	34.05	23.17	0.00	16.59	0.00

According to Table 4, FRE2, YRO, Y4R, and HTCD were plagued by pixels with negative powers, whereas this problem was not encountered in the decomposition results of either GRH or MF4CF. For FRE2, there were negative power pixels in all three components (*Pd*, *Pv*, and *Ps*), which is due to confusion in scattering characteristic modeling as shown in Figure 3f. For model-based decomposition methods, such as YRO and Y4R, negative scattering powers typically occur in surface scattering or double-bounce scattering components. The Yamaguchi volume scattering model assumes one dimension of needle-like scatters to be zero, which may cause overestimation of the volume scattering component, resulting in negative power pixels in the double-bounce scattering component and/or surface scattering component. Eigenvalue-based HTCD polarization decomposition was performed by calculating the eigenvalues of the coherency matrix from the scattering model of each model. The choice of scattering model affected the value of the eigenvalues, and there were also many negative pixels due to the unfit scattering models.

MF4CF and GRH were the only algorithms to produce almost no negative pixels in our test. MF4CF used the depolarization coefficient (calculated from the 3-D Barakat degree of polarization) to derive the volume scattering component, and it was considered that the depolarization component corresponded to the volume scattering component. However, the algorithm considered that the double-bounce scattering components and the surface scattering components contained no depolarization components, which sacrificed the depolarization accuracy to avoid pixels with negative powers. The GRH in this paper

can avoid pixels with negative powers because separate modeling of different scattering mechanisms can be adapted to the characteristics of the data.

4. Conclusions

Previous studies have shown that the existing methods commonly encounter problems regarding the polarimetric decomposition accuracy and pixels with negative powers, the main reason for which is that most volume scattering models are empirical models based on data or simplified assumptions, resulting that the dynamic range of the model itself is limited and cannot fully satisfy the mixed scenario. In this paper, we propose a hybrid polarimetric decomposition method (GRH) with an adaptive volume scattering model. The volume scattering model is proposed by considering the shape and distribution of the scattered particles based on the physical scattering characteristics. This is the first model-based adaptive model proposed to characterize the volume scattering component in regions dominant by different scattering mechanisms using adaptive scattering models. In other words, GRH adaptively selects either the GVSM or the RPCM according to the dominant scattering mechanisms in the target area. In contrast to existing adaptive models, the volume scattering model of GRH varies according to the dominant scattering mechanisms of surface or double-bounce scattering. GRH identifies the dominant scattering mechanisms using the sign of $(T_{11} - T_{22})$: If $(T_{11} - T_{22}) \geq 0$, GRH selects RPCM to calculate the decomposition components; otherwise, GRH selects GVSM.

We tested GRH using 4-look fully PolSAR data and compared its performance with that of both existing classic and new algorithms. The results showed that the proposed method can extract reasonable scattering components and considerably reduce the percentage of pixels with negative powers, demonstrating the effectiveness of the adaptive volume scattering model.

The proposed method provides a new approach to selecting scattering models to improve decomposition accuracy and reduce negative power pixels, which selects scattering models according to scattering characteristics. Further research may focus on exploring new models that fit specific targets, such as ships, bridges, and forests, following this framework.

Author Contributions: Conceptualization, X.L. (Xiujuan Li) and Y.L.; methodology, X.L. (Xiujuan Li) and P.H.; software, X.L. (Xiujuan Li) and Y.L.; investigation, X.L. (Xiaolong Liu) and W.F.; visualization, X.L. (Xiujuan Li) and X.L. (Xiaolong Liu); writing—original draft preparation, X.L. (Xiujuan Li) and X.L. (Xiaolong Liu); writing—review and editing, Y.L., P.H. and W.T.; project administration, Y.L. and C.L. All authors have read and agreed to the published version of the manuscript.

Funding: This work was supported in part by the National Natural Science Foundation of China under Grant (Nos. 61971417 and Nos. 52064039); in part by the Science and Technology Innovation Guidance Project of Inner Mongolia Autonomous Region (Nos. 2019GG138, Nos. 2019GG139 and 2020GG0073); and in part by the Science and Technology Major Special Project of Inner Mongolia Autonomous Region (Nos. 2019ZD022).

Data Availability Statement: Not applicable.

Acknowledgments: The authors would like to thank Chufeng Hu from Northwestern Polytechnical University for the kind suggestions on the expressions used in the manuscript.

Conflicts of Interest: The authors declare no conflict of interest.

References

1. Chen, S.; Wang, X.; Xiao, S. Urban damage level mapping based on co-polarization coherence pattern using multitemporal polarimetric SAR data. *IEEE J. Sel. Top. Appl. Earth Obs. Remote Sens.* **2018**, *11*, 2657–2667. [CrossRef]
2. Ji, Y.; Sri Sumantyo, J.T.; Chua, M.Y.; Waqar, M.M. Earthquake/tsunami damage assessment for urban areas using post-event PolSAR data. *Remote Sens.* **2018**, *10*, 1088. [CrossRef]
3. Musthafa, M.; Khati, U.; Singh, G. Sensitivity of PolSAR decomposition to forest disturbance and regrowth dynamics in a managed forest. *Adv. Space Res.* **2020**, *66*, 1863–1875. [CrossRef]

4. Varghese, A.O.; Suryavanshi, A.; Joshi, A.K. Analysis of different polarimetric target decomposition methods in forest density classification using C band SAR data. *Int. J. Remote Sens.* **2016**, *37*, 694–709. [CrossRef]
5. Acar, H.; Ozerdem, M.S.; Acar, E. Soil moisture inversion via semiempirical and machine learning methods with full-polarization Radarsat-2 and polarimetric target decomposition data: A comparative study. *IEEE Access* **2020**, *8*, 197896–197907. [CrossRef]
6. Zhang, L.; Meng, Q.; Zeng, J.; Wei, X.; Shi, H. Evaluation of Gaofen-3 C-band SAR for soil moisture retrieval using different polarimetric decomposition models. *IEEE J. Sel. Top. Appl. Earth Obs. Remote Sens.* **2021**, *14*, 5707–5719. [CrossRef]
7. Tan, W.; Sun, B.; Xiao, C.; Huang, P.; Xu, W.; Yang, W. A novel unsupervised classification method for sandy land using fully polarimetric SAR data. *Remote Sens.* **2021**, *13*, 355. [CrossRef]
8. Maurya, H.; Panigrahi, R.K. Non-negative scattering power decomposition for PolSAR data interpretation. *IET Radar Sonar Navig.* **2018**, *12*, 593–602. [CrossRef]
9. Arii, M.; van Zyl, J.J.; Kim, Y. A general characterization for polarimetric scattering from vegetation canopies. *IEEE Trans. Geosci. Remote Sens.* **2010**, *48*, 3349–3357. [CrossRef]
10. Wang, Y.; Yu, W.; Wang, C.; Liu, X. A modified four-component decomposition method with refined volume scattering models. *IEEE J. Sel. Top. Appl. Earth Obs. Remote Sens.* **2020**, *13*, 1946–1958. [CrossRef]
11. Zhang, S.; YU, X.; WANG, L. Modified version of three-component model-based decomposition for polarimetric SAR data. *J. Syst. Eng. Electron.* **2019**, *30*, 270–277. [CrossRef]
12. Sato, A.; Yamaguchi, Y.; Singh, G.; Sang-Eun, P. Four-component scattering power decomposition with extended volume scattering model. *IEEE Geosci. Remote Sens. Lett.* **2012**, *9*, 166–170. [CrossRef]
13. Kumar, A.; Maurya, H.; Misra, A.R.; Panigrahi, R.K. An Improved Decomposition as a Trade-Off between Utilizing Unitary Matrix Rotations and New Scattering Models. *IEEE Access* **2021**, *9*, 77482–77492. [CrossRef]
14. Chen, S.; Li, Y.; Wang, X.; Xiao, S.; Sato, M. Modeling and Interpretation of Scattering Mechanisms in Polarimetric Synthetic Aperture Radar: Advances and perspectives. *IEEE Signal. Process. Mag.* **2014**, *31*, 79–89. [CrossRef]
15. Van Zyl, J.J.; Arii, M.; Kim, Y. Model-based decomposition of polarimetric SAR covariance matrices constrained for nonnegative eigenvalues. *IEEE Trans. Geosci. Remote Sens.* **2011**, *49*, 3452–3459. [CrossRef]
16. Van Zyl, J.J.; Arii, M.; Kim, Y. Requirements for Model-Based Polarimetric Decompositions. In Proceedings of the International Geoscience and Remote Sensing Symposium (IGARSS), Boston, MA, USA, 8–11 July 2008; IEEE: New York, NY, USA, 2008; Volume 5, pp. V-417–V-420.
17. Freeman, A.; Durden, S.L. A three-component scattering model for polarimetric SAR data. *IEEE Trans. Geosci. Remote Sens.* **1998**, *36*, 963–973. [CrossRef]
18. Yamaguchi, Y.; Yajima, Y.; Yamada, H. A four-component decomposition of PoLSAR images based on the coherency matrix. *IEEE Geosci. Remote Sens. Lett.* **2006**, *3*, 292–296. [CrossRef]
19. Wang, Z.; Zeng, Q.; Jiao, J. A New Volume Scattering Model for Three-Component Decomposition of Polarimetric SAR Data. *Int. Geosci. Remote Sens. Symp.* **2018**, *2018*, 4575–4578. [CrossRef]
20. Yin, Q.; Xu, J.; Xiang, D.; Zhou, Y.; Zhang, F. Polarimetric Decomposition with an Urban Area Descriptor for Compact Polarimetric SAR Data. *IEEE J. Sel. Top. Appl. Earth Obs. Remote Sens.* **2021**, *14*, 10033–10044. [CrossRef]
21. Yamaguchi, Y.; Moriyama, T.; Ishido, M.; Yamada, H. Four-component scattering model for polarimetric SAR image decomposition. *IEEE Trans. Geosci. Remote Sens.* **2005**, *43*, 1699–1706. [CrossRef]
22. Singh, G.; Malik, R.; Mohanty, S.; Rathore, V.S.; Yamada, K.; Umemura, M.; Yamaguchi, Y. Seven-component scattering power decomposition of PoLSAR coherency matrix. *IEEE Trans. Geosci. Remote Sens.* **2019**, *57*, 8371–8382. [CrossRef]
23. Singh, G.; Yamaguchi, Y. Model-based six-component scattering matrix power decomposition. *IEEE Trans. Geosci. Remote Sens.* **2018**, *56*, 5687–5704. [CrossRef]
24. Han, W.; Fu, H.; Zhu, J.; Wang, C.; Xie, Q. Polarimetric SAR Decomposition by Incorporating a Rotated Dihedral Scattering Model. *IEEE Geosci. Remote Sens. Lett.* **2022**, *19*, 4005505. [CrossRef]
25. Wang, Y.; Ainsworth, T.L.; Lee, J. Sen Disk-Shaped Random Scatterers with Application to Model-Based PolSAR Decomposition. *IEEE Geosci. Remote Sens. Lett.* **2021**, *18*, 1961–1965. [CrossRef]
26. Yin, J.; Yang, J. Target Decomposition Based on Symmetric Scattering Model for Hybrid Polarization SAR Imagery. *IEEE Geosci. Remote Sens. Lett.* **2021**, *18*, 494–498. [CrossRef]
27. Yamaguchi, Y.; Sato, A.; Boerner, W.; Sato, R.; Yamada, H. Four-component scattering power decomposition with rotation of coherency matrix. *IEEE Trans. Geosci. Remote Sens.* **2011**, *49*, 2251–2258. [CrossRef]
28. Maurya, H.; Panigrahi, R.K. PolSAR coherency matrix optimization through selective unitary rotations for model-based decomposition scheme. *IEEE Geosci. Remote Sens. Lett.* **2019**, *16*, 658–662. [CrossRef]
29. Chen, S.; Wang, X.; Xiao, S.; Sato, M. General polarimetric model-based decomposition for coherency matrix. *IEEE Trans. Geosci. Remote Sens.* **2014**, *52*, 1843–1855. [CrossRef]
30. Ainsworth, T.L.; Wang, Y.; Lee, J. Sen Model-Based Polarimetric SAR Decomposition: An L1 Regularization Approach. *IEEE Trans. Geosci. Remote Sens.* **2022**, *60*, 1–13. [CrossRef]
31. Van Zyl, J.J. Application of Cloude's Target Decomposition Theorem to Polarimetric Imaging Radar Data. *Radar Polarim.* **1993**, *1748*, 184. [CrossRef]
32. Arii, M.; van Zyl, J.J.; Kim, Y. Adaptive model-based decomposition of polarimetric sar covariance matrices. *IEEE Trans. Geosci. Remote Sens.* **2011**, *49*, 1104–1113. [CrossRef]

33. Cui, Y.; Yamaguchi, Y.; Yang, J.; Park, S.; Kobayashi, H.; Singh, G. Three-component power decomposition for polarimetric SAR data based on adaptive volume scatter modeling. *Remote Sens.* **2012**, *4*, 1559–1572. [CrossRef]
34. Bhattacharya, A.; Singh, G.; Manickam, S.; Yamaguchi, Y. An adaptive general four-component scattering power decomposition with unitary transformation of coherency matrix (AG4U). *IEEE Geosci. Remote Sens. Lett.* **2015**, *12*, 2110–2114. [CrossRef]
35. Wang, X.; Zhang, L.; Zhu, S. A Four-Component Decomposition Model for Polarimetric SAR Images Based on Adaptive Volume Scattering Model. In Proceedings of the IGARSS 2018—2018 IEEE International Geoscience and Remote Sensing Symposium, Valencia, Spain, 23–27 July 2018; pp. 4563–4566.
36. Xie, Q.; Zhu, J.; Lopez-Sanchez, J.M.; Wang, C.; Fu, H. A modified general polarimetric model-based decomposition method with the simplified neumann volume scattering model. *IEEE Geosci. Remote Sens. Lett.* **2018**, *15*, 1229–1233. [CrossRef]
37. Wang, Z.; Zeng, Q.; Jiao, J. An adaptive decomposition approach with dipole aggregation model for polarimetric sar data. *Remote Sens.* **2021**, *13*, 2583. [CrossRef]
38. Antropov, O.; Rauste, Y.; Hame, T. Volume scattering modeling in PolSAR decompositions: Study of ALOS PALSAR data over boreal forest. *IEEE Trans. Geosci. Remote Sens.* **2011**, *49*, 3838–3848. [CrossRef]
39. Freeman, A. Fitting a two-component scattering model to polarimetric SAR data from forests. *IEEE Trans. Geosci. Remote Sens.* **2007**, *45*, 2583–2592. [CrossRef]
40. Dey, S.; Bhattacharya, A.; Frery, A.C.; Lopez-Martinez, C.; Rao, Y.S. A model-free four component scattering power decomposition for polarimetric SAR data. *IEEE J. Sel. Top. Appl. Earth Obs. Remote Sens.* **2021**, *14*, 3887–3902. [CrossRef]
41. Nghiem, S.; Yueh, S.; Kwok, R.; Nguyen, D. Polarimetric remote sensing of geophysical medium structures. *Radio Sci.* **1993**, *28*, 1111–1130. [CrossRef]
42. Neumann, M.; Ferro-Famil, L.; Reigber, A. Estimation of forest structure, ground, and canopy layer characteristics from multibaseline polarimetric interferometric SAR data. *IEEE Trans. Geosci. Remote Sens.* **2010**, *48*, 1086–1104. [CrossRef]
43. Dong, Z.; Feng, X.; Zhou, H.; Liu, C.; Sato, M. Effects of induced field rotation from rough surface on H-alpha decomposition of full-polarimetric GPR. *IEEE Trans. Geosci. Remote Sens.* **2021**, *59*, 9192–9208. [CrossRef]
44. Lee, J.; Pottier, E. *Polarimetric Radar Imaging: From Basics to Applications*; CRC Press/Taylor & Francis: Boca Raton, FL, USA, 2009.
45. An, W.; Cui, Y.; Yang, J. Three-component model-based decomposition for polarimetric sar data. *IEEE Trans. Geosci. Remote Sens.* **2010**, *48*, 2732–2739. [CrossRef]